


Article

Immunosensor with Enhanced Electrochemiluminescence Signal Using Platinum Nanoparticles Confined within Nanochannels for Highly Sensitive Detection of Carcinoembryonic Antigen

Huihua Zhang ^{1,2,*}, Chaoyan Zhang ³, Hui Qu ^{1,2} and Fengna Xi ^{3,*} 

¹ Shanxi Bethune Hospital, Shanxi Academy of Medical Sciences, Tongji Shanxi Hospital, Third Hospital of Shanxi Medical University, Taiyuan 030032, China; quhui1986@hotmail.com

² Tongji Hospital, Tongji Medical College, Huazhong University of Science and Technology, Wuhan 430030, China

³ School of Chemistry and Chemical Engineering, Zhejiang Sci-Tech University, Hangzhou 310018, China; 202130107346@mails.zstu.edu.cn

* Correspondence: ykdzhanghuihua1008@sxmu.edu.cn (H.Z.); fengnaxi@zstu.edu.cn (F.X.)

Abstract: Rapid, highly sensitive, and accurate detection of tumor biomarkers in serum is of great significance in cancer screening, early diagnosis, and postoperative monitoring. In this study, an electrochemiluminescence (ECL) immunosensing platform was constructed by enhancing the ECL signal through in situ growth of platinum nanoparticles (PtNPs) in a nanochannel array, which can achieve highly sensitive detection of the tumor marker carcinoembryonic antigen (CEA). An inexpensive and readily available indium tin oxide (ITO) glass electrode was used as the supporting electrode, and a layer of amino-functionalized vertically ordered mesoporous silica film (NH₂-VMSF) was grown on its surface using an electrochemically assisted self-assembly method (EASA). The amino groups within the nanochannels served as anchoring sites for the one-step electrodeposition of PtNPs, taking advantage of the confinement effect of the ultrasmall nanochannels. After the amino groups on the outer surface of NH₂-VMSF were derivatized with aldehyde groups, specific recognition antibodies were covalently immobilized followed by blocking nonspecific binding sites to create an immunorecognition interface. The PtNPs, acting as nanocatalysts, catalyzed the generation of reactive oxygen species (ROS) with hydrogen peroxide (H₂O₂), significantly enhancing the ECL signal of the luminol. The ECL signal exhibited high stability during continuous electrochemical scanning. When the CEA specifically bound to the immunorecognition interface, the resulting immune complexes restricted the diffusion of the ECL emitters and co-reactants towards the electrode, leading to a reduction in the ECL signal. Based on this immune recognition-induced signal-gating effect, the immunosensor enabled ECL detection of CEA with a linear range of 0.1 pg mL⁻¹ to 1000 ng mL⁻¹ with a low limit of detection (LOD, 0.03 pg mL⁻¹). The constructed immunosensor demonstrated excellent selectivity and can achieve CEA detection in serum.

Keywords: immunosensor; electrochemiluminescence; confined nanocatalyst; signal enhancement; carcinoembryonic antigen



Citation: Zhang, H.; Zhang, C.; Qu, H.; Xi, F. Immunosensor with Enhanced Electrochemiluminescence Signal Using Platinum Nanoparticles Confined within Nanochannels for Highly Sensitive Detection of Carcinoembryonic Antigen. *Molecules* **2023**, *28*, 6559. <https://doi.org/10.3390/molecules28186559>

Academic Editors: Liqiang Luo, Ruilin Liu, Huiping Sun and Chunsheng Wu

Received: 16 August 2023

Revised: 1 September 2023

Accepted: 5 September 2023

Published: 11 September 2023



Copyright: © 2023 by the authors. Licensee MDPI, Basel, Switzerland. This article is an open access article distributed under the terms and conditions of the Creative Commons Attribution (CC BY) license (<https://creativecommons.org/licenses/by/4.0/>).

1. Introduction

Carcinoembryonic antigen (CEA) is a glycoprotein involved in cell adhesion and is originally extracted from the human colon and embryonic tissues [1,2]. It has been proven that CEA is expressed during fetal development in humans, but its expression levels are suppressed to relatively low levels after birth and during growth. However, in certain malignant tumor patients, especially those with colorectal cancer, CEA can circulate in the bloodstream in high concentrations. Other malignancies, such as melanoma, gastric cancer, breast cancer, ovarian cancer, lung cancer, and pancreatic cancer, may also result in elevated CEA levels. Therefore, CEA serves as an important broad-spectrum tumor biomarker with

widespread applications in cancer screening, early diagnosis, and postoperative monitoring [3–5]. For example, changes in CEA levels can be used to evaluate the effectiveness of treatment, predict patient prognosis, and monitor cancer recurrence. Therefore, rapid, highly sensitive, and accurate detection of CEA in serum is of great significance.

Immunoassay is the most commonly used strategy for CEA determination that detects the signal changes caused by the binding of CEA and specific antibodies. Depending on the signal, methods including the enzyme-linked immunosorbent assay (ELISA) [6], radioimmunoassay (RIA), chemiluminescence immunoassay (CLIA) [7], electrochemical immunoassay [8–11], and electrochemiluminescence (ECL) immunoassay [12,13] have been developed. However, an ELISA usually requires a longer detection time and may be influenced by interfering factors. An RIA involves radioactive substances. Chemiluminescence has advantages, such as high sensitivity, a short detection time, and a high level of automation, but it suffers from strict requirements for sample handling and storage. Electrochemical methods offer fast and sensitive detection, but reproducibility remains a challenge. In recent years, ECL technology, also known as electrogenerated chemiluminescence, has gained widespread attention due to its low background, high sensitivity, fast detection speed, and low cost [14–18]. As a technique that combines electrochemistry with chemiluminescence, ECL refers to the generation of luminescent species by inducing high-energy electron transfer reactions on the electrode surface through applied voltage. Until now, a luminol-based ECL system that uses luminol as the luminescent reagent and hydrogen peroxide (H_2O_2) as a co-reactant has been widely used in fields such as bioanalysis, environmental testing, and chemical sensing [19,20]. On the one hand, luminol loses a proton to become the luminol anion in an alkaline environment, then undergoes electrochemical oxidation to form the luminol radical. On the other hand, the electrochemical oxidation of H_2O_2 generates reactive oxygen species (ROS). Then, the luminol radical reacts with ROS to reach the excited state and emits light when it returns to the ground state. Promoting the generation of ROS during the ECL process is effective at enhancing the sensitivity of the luminol-based ECL sensors.

So far, various materials have been used as catalysts to enhance the detection performance of the sensing platform [21–24]. Among them, noble metal nanomaterials have attracted wide attention due to their large surface area, excellent conductivity, and high catalytic activity [20–22]. For example, platinum (Pt) nanomaterials have good catalytic activity and surface characteristics, enabling the catalysis of H_2O_2 to generate ROS [25–30]. Commonly, the surface of Pt nanomaterials contains many active sites where Pt atoms can react with H_2O_2 molecules, causing localized oxidation and reduction reactions of oxygen and hydrogen atoms. At the same time, Pt nanomaterials can facilitate the decomposition of H_2O_2 , thereby forming ROS. However, Pt nanomaterials prepared by traditional chemical synthesis methods tend to aggregate. In situ growth of noble metal nanomaterials within confined nanospaces allows for the production of high-performance nanocatalysts [31,32]. Specifically, confined spaces can restrict the diffusion and aggregation of reactants, allowing reactions to occur in very small areas. Thus, control of the size and morphology of noble metal nanomaterials can be achieved in a more uniform nucleation and growth process. In addition, due to the higher surface area-to-volume ratio provided by confined spaces, in situ synthesized noble metal nanomaterials have more active sites and surface reactivity, thereby enhancing their catalytic activity. Therefore, in situ preparation of noble metal nanocatalysts within confined spaces provides new possibilities for the fabrication of highly sensitive ECL sensors.

The growth of vertically ordered mesoporous silica nanochannel film (VMSF) on the electrode surface is an important approach for constructing nanostructured electrodes [33–36]. Currently, large-area VMSF-modified electrodes (e.g., tens of square centimeters) can be conveniently prepared using the Stöber solution growth method [37–41]. Alternatively, electrochemically assisted self-assembly (EASA) can be used to rapidly grow VMSF on the electrode surface within 5–30 s [42–44]. VMSF possesses an array of ultra-small nanochannels perpendicular to the substrate electrode with channel diam-

eters typically in the range of 2–3 nanometers and a film thickness adjustable between 20–200 nanometers [45,46]. The high density of the nanochannels can reach up to 75,000 per square micrometer [47–49]. Thus, VMSF has a robust and three-dimensional (3D) silica framework with the nanochannels integrated with the external surface. This unique structure of VMSF confers several advantages to the modified electrode. On the one hand, the VMSF modification layer exhibits minimal swelling during use, greatly enhancing the stability and reproducibility of the modified electrode [50,51]. Furthermore, VMSF includes two independent modification regions, including the nanochannel array and the outer surface. This makes it easier to integrate multifunctionality into the electrode. For example, the nanochannel array of VMSF can serve as a carrier for immobilizing a large amount of stable nanocatalysts, while the outer surface of VMSF can be used to immobilize antibodies or other biorecognition ligands. By spatially separating the processes of immunorecognition and ECL emission, functional integration is achieved under the diffusion of small molecules in the external solution. Based on the 3D structure of VMSF, the integration of in situ grown nanocatalysts and immunorecognition interfaces holds promise for the preparation of high-performance ECL immunosensors.

In this study, an ECL immunosensing platform for the highly sensitive detection of CEA was constructed by functionalizing nanochannels and the outer surface of VMSF. Amino-functionalized VMSF (NH_2 -VMSF) was rapidly grown on an inexpensive and readily available indium tin oxide (ITO) electrode using an electrochemically assisted self-assembly method (EASA). The amino groups inside the nanochannels served as anchoring sites for the in situ electrodeposition of the platinum nanoparticles (PtNPs) via one-step electrodeposition, while the amino groups on the outer surface were applied for the covalent immobilization of recognition antibodies after aldehyde derivatization, forming an immunorecognition interface. Due to the catalytic activity of PtNPs in decomposing H_2O_2 to generate ROS, the ECL signal of the luminol– H_2O_2 system was significantly enhanced and exhibited high stability. When CEA was present, its binding on the immunorecognition interface formed large-sized immunocomplexes, which hindered the diffusion of the luminescent species and co-reactant to the underlying electrode surface, resulting in a decrease in the ECL signal. Based on the signal-gating effect induced by the immunorecognition, the detection of CEA with high sensitivity could be achieved.

2. Results and Discussion

2.1. Construction of Immunosensors and Signal-Gated ECL Detection

Figure 1 is the schematic illustration of the fabrication of the immunosensor and CEA detection. As shown, the indium tin oxide (ITO) electrode was used as the supporting electrode for the immunosensor fabrication. As a transparent conductive material widely used in modern electronic devices, the ITO electrode exhibits good conductivity, low resistance, excellent corrosion resistance, and stability. Additionally, ITO electrodes are suitable for patterning, making them highly promising for low-cost, disposable sensor devices. As demonstrated, a layer of NH_2 -VMSF was grown on the clean ITO surface using the traditional electrochemical-assisted self-assembly (EASA) method. This method combines electrochemical deposition and self-assembly techniques by applying a negative potential to the electrode, inducing a pH gradient on the electrode surface through reducing hydrogen ions. This gradient facilitates the self-assembly of surfactant micelles (SMs) and the sol–gel process of siloxane precursors on the electrode surface. The resulting film is enriched with amino groups due to the use of amino-functionalized siloxane precursors and contains surfactant micelles within the formed pores ($\text{SM}@\text{NH}_2\text{-VMSF/ITO}$). The surfactant micelles can be easily removed by immersing the $\text{SM}@\text{NH}_2\text{-VMSF/ITO}$ in a hydrochloric acid–ethanol solution, yielding an array of open nanochannels. To immobilize the antibodies (Abs) on the outer surface of the VMSF, the amino groups were modified using glutaraldehyde (GA), which generated aldehyde groups for covalent antibody immobilization. To prevent GA from entering the nanochannels and affecting the permeability, a strategy involving GA derivatization followed by SM removal was employed to ensure that

aldehyde derivatization occurred only on the outer surface of the NH_2 -VMSF. Subsequently, PtNPs were electro-deposited in situ within the nanochannels. The amino sites within the nanochannels served as anchoring points for the growth of PtNPs, improving their stability. Finally, CEA antibodies were covalently immobilized on the aldehyde-functionalized surface, and after blocking nonspecific sites with BSA, the immunosensor was obtained ($\text{Ab/GA/PtNPs/NH}_2\text{-VMSF/ITO}$). It can be observed that in the 3D structure of the NH_2 -VMSF, the outer surface and nanochannels are divided into two independent functional domains. The outer surface serves as the immunorecognition interface, while the PtNPs deposited inside the nanochannels act as nanocatalysts.

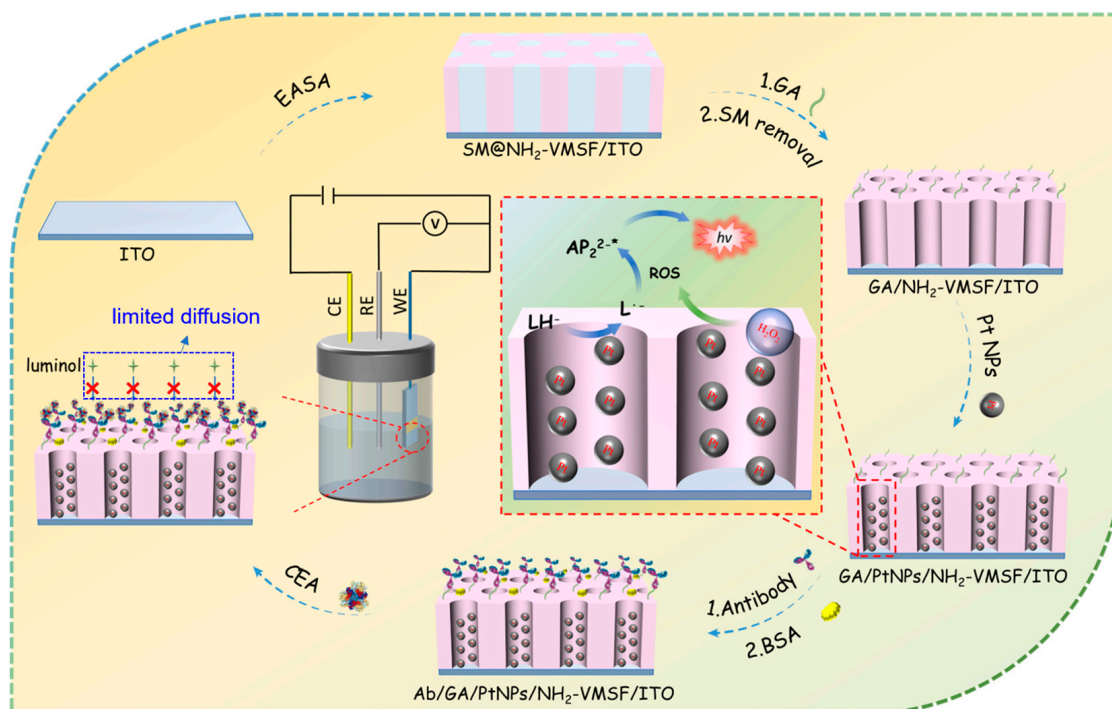


Figure 1. Schematic illustration of the fabrication of the immunosensor and CEA detection based on immunorecognition-induced signal gating phenomenon.

For CEA detection, luminol was used as the ECL emitter and H_2O_2 was employed as the co-reactant of the luminol, while the PtNPs served as the co-reactant promoter or an effective catalyst for the H_2O_2 . They facilitated the electrocatalytic generation of a large amount of ROS, which reacts with the luminescent radical generated by the electrochemical oxidation of the luminol, leading to the formation of excited-state luminol and the subsequent emission of light. Thus, the catalytic effect of PtNPs can effectively enhance the ECL signal intensity in the luminol– H_2O_2 system, thereby improving the detection sensitivity. When CEA is present, antibodies on the immunorecognition interface can selectively capture CEA, forming an immunocomplex. The spatial hindrance effect caused by the immunocomplex reduces the diffusion of luminol and H_2O_2 toward the surface of the electrode, thus decreasing the ECL signal. Based on this immunorecognition-induced signal-gating phenomenon, ECL detection of CEA can be achieved.

2.2. Characterization of NH_2 -VMSF

TEM and SEM were used to characterize the morphology of NH_2 -VMSF/ITO. The top-view TEM image in Figure 2a reveals that the nanopores are well-ordered and arranged in a hexagonal array. No cracks or fractures are observed within the observed area. The pore size is uniform, measuring approximately 2–3 nm. The cross-sectional SEM image of the VMSF/ITO electrode was also investigated. Due to the non-conductivity of both the glass and VMSF layers, a gold spraying treatment is required before SEM characterization,

resulting in the indistinct density difference among the glass, ITO, and VMSF layers. However, the SEM image in Figure 2b still reveals the three-layer structure of the VMSF, ITO, and glass from top to bottom. The thickness of NH₂-VMSF is approximately 88 nm.

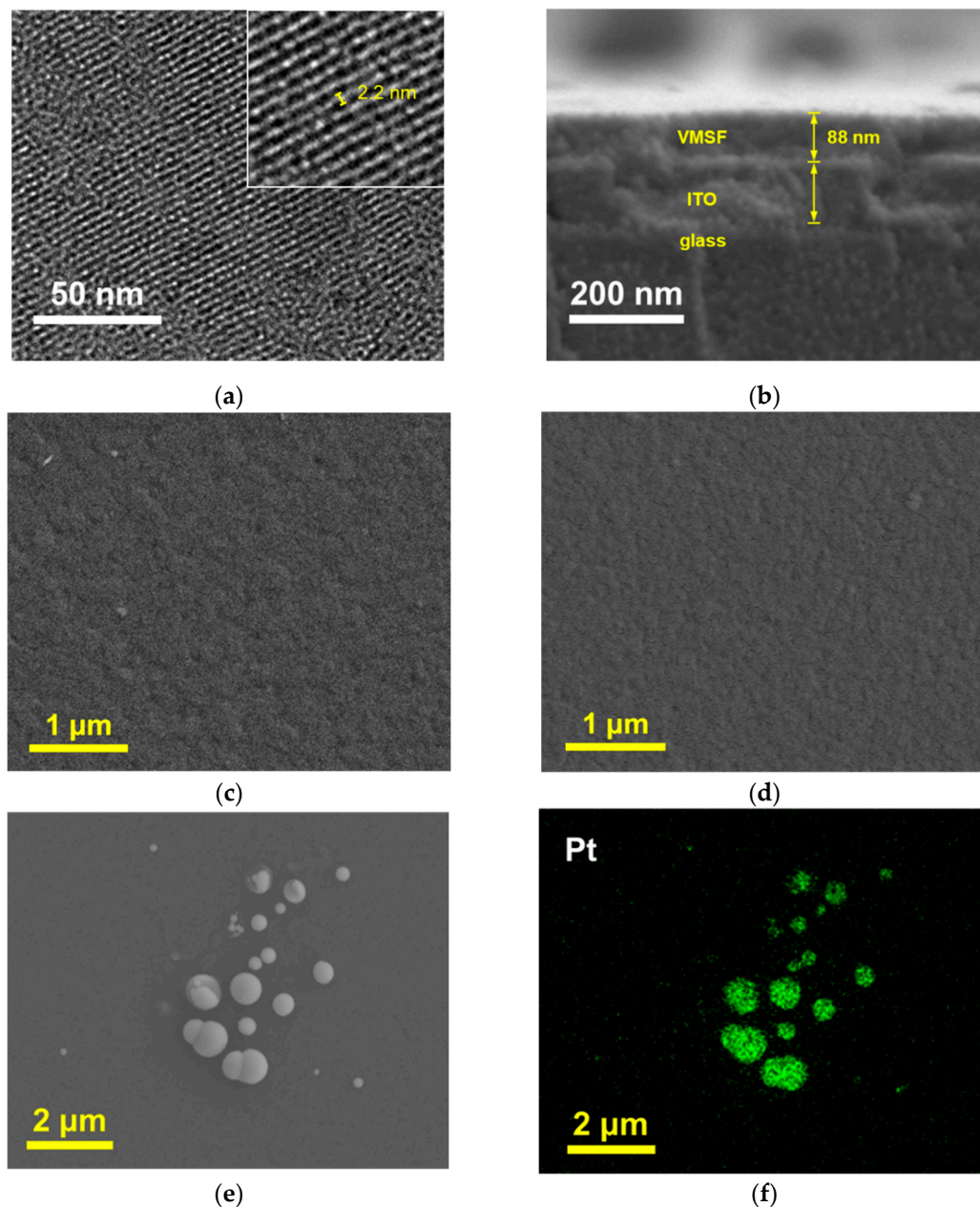


Figure 2. (a) Top-view TEM image of NH₂-VMSF. Inset is the high-resolution TEM image. (b) Cross-sectional SEM image of NH₂-VMSF/ITO. (c,d) Top-view of SEM image of NH₂-VMSF/ITO (c) and PtNPs@NH₂-VMSF/ITO (d). (e,f) SEM image (e) and elemental mapping (f) of the electrode obtained after NH₂-VMSF on PtNPs@NH₂-VMSF/ITO was removed by dissolution with NaOH solution.

2.3. Characterization of PtNPs@NH₂-VMSF

In order to verify the successful modification of the PtNPs inside the nanochannels, SEM was used to characterize different electrodes. As shown in Figure 2c, the NH₂-VMSF/ITO electrode without PtNP deposition exhibits a flat surface. Upon PtNP modification, there was no significant change in the surface morphology of the electrode, indicating an absence of large nanostructures formed on the outer surface of NH₂-VMSF (Figure 2d). To further confirm this, the NH₂-VMSF layer on the PtNPs@NH₂-VMSF/ITO electrode was dissolved and removed using NaOH, followed by SEM characterization of the result-

ing electrode surface. As shown in Figure 2e, numerous spherical structures of varying sizes appear on the ITO substrate, and elemental mapping confirms that these spherical structures correspond to Pt materials (Figure 2f). This can be attributed to the fact that, when $\text{NH}_2\text{-VMSF/ITO}$ is dissolved, PtNPs lose their protection from the nanochannels and undergo aggregation, thus confirming that the electrodeposited PtNPs are confined within the nanochannels.

XPS analysis was further conducted on the $\text{PtNPs@NH}_2\text{-VMSF/ITO}$ electrode to determine its elemental composition. Figure 3a shows the XPS survey spectrum, which reveals significant peaks corresponding to O, Si, Pt, and N elements. Figure 3b presents the high-resolution Pt_{4f} spectrum with two strong peaks observed at around 71.5 eV and 75.4 eV, confirming the presence of platinum. The results confirm the presence of amino-functionalized silica structures and deposited Pt nanoparticles in the $\text{PtNPs@NH}_2\text{-VMSF}$ modification layer.

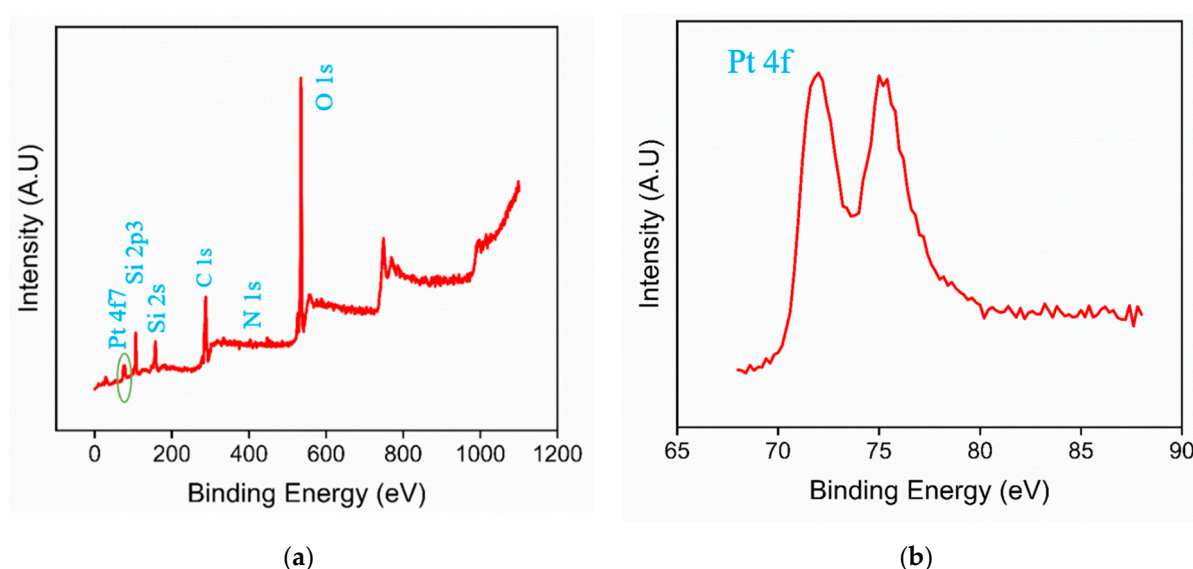


Figure 3. XPS survey spectrum (a) and high-resolution Pt_{4f} spectrum (b) of $\text{PtNPs@NH}_2\text{-VMSF/ITO}$.

2.4. The Enhanced ECL by PtNPs

The influence of PtNP deposition time on the ECL performance of the electrode was examined. As shown in Figure 4a, the ECL intensities of $\text{PtNPs@NH}_2\text{-VMSF/ITO}$ electrodes obtained with different deposition times were compared. The results reveal that the ECL intensity of the electrode initially increases and then decreases with increasing PtNP deposition time. This may be attributed to the fact that a longer deposition time can increase the amount of deposited PtNPs, but an excessively large nanoparticle size due to prolonged deposition time could decrease the diffusion of ECL emitters and co-reactants inside the nanochannels, resulting in reduced ECL intensity. To achieve the highest ECL signal, the electrode with a PtNP deposition time of 2 s was selected for further experiments. Compared to $\text{NH}_2\text{-VMSF/ITO}$ electrodes without nanocatalysts, the ECL response measured on $\text{PtNPs@NH}_2\text{-VMSF/ITO}$ electrodes was enhanced four-fold.

ECL measurements at different scan potential ranges were further conducted on the electrodes before and after PtNP deposition to further validate the catalytic effect of PtNPs. When the scan potential range was set from 0 V to 0.8 V, the electrode with PtNP deposition exhibited a certain improvement in ECL signal compared to the unmodified $\text{NH}_2\text{-VMSF/ITO}$ electrode (Figure 4b). However, the enhancement of the ECL signal was not significant. On the contrary, when the initial scan potential was shifted to -1 V, the ECL signal of the $\text{PtNPs@NH}_2\text{-VMSF/ITO}$ electrode showed a remarkable increase. This demonstrates that the significant enhancement in the ECL signal is attributed to the electrocatalysis of H_2O_2 by the PtNPs at negative potentials.

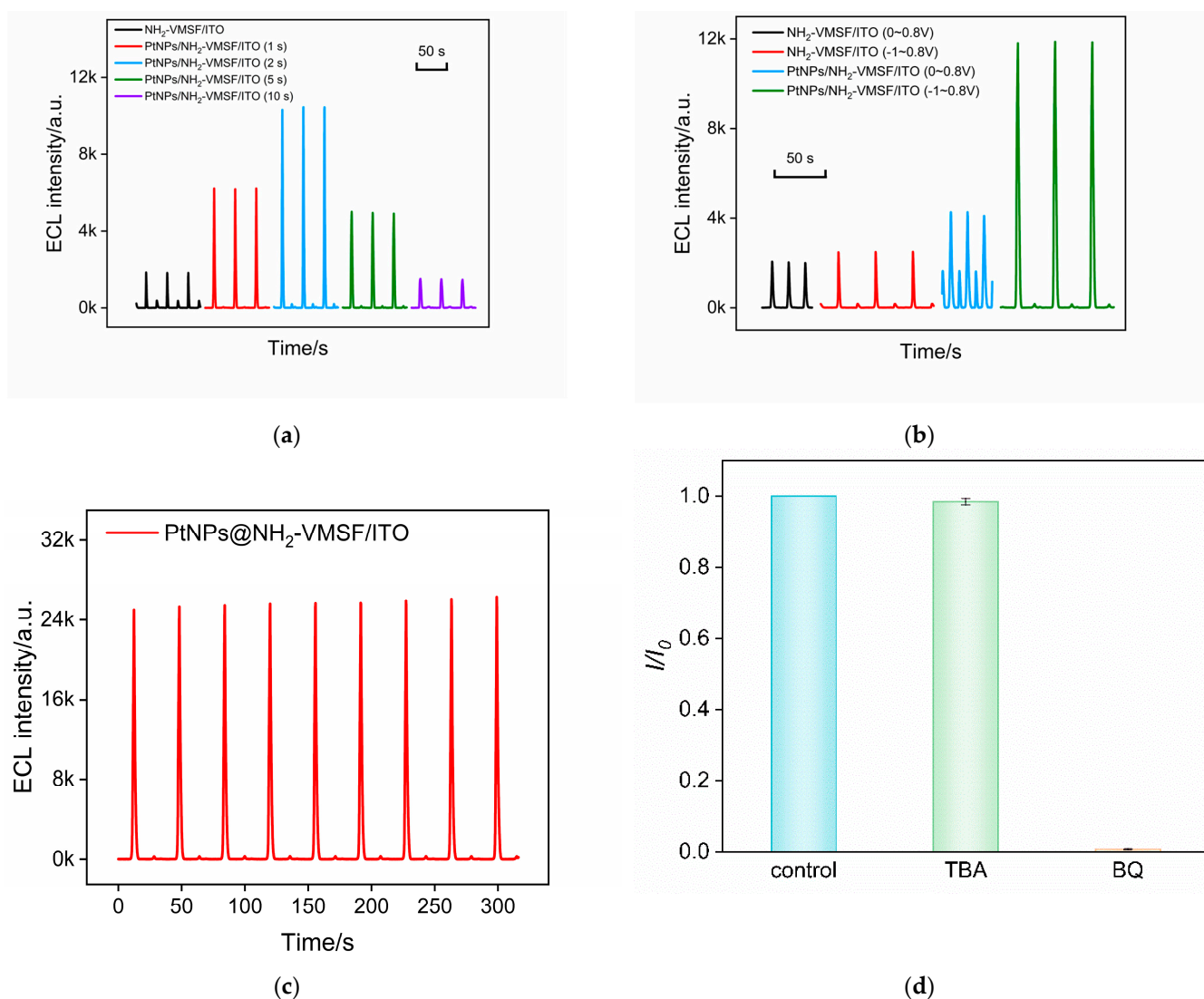
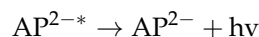
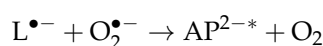
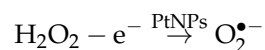
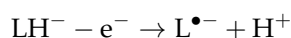


Figure 4. (a) ECL signal obtained on PtNPs/NH₂-VMSF/ITO electrode prepared using different deposition times for the in situ synthesis of PtNPs. (b) ECL signal obtained on PtNPs/NH₂-VMSF/ITO electrode under different potential ranges. (c) ECL signal under continuous CV scanning. (d) The relative ratio of ECL intensity in absence (I_0) or presence (I) of different free radical scavengers.

To examine the stability of the ECL signal, the electrode was subjected to continuous electrochemical scans, and its ECL signal was recorded. As shown in Figure 4c, there was no significant change in the ECL signal of the PtNPs@NH₂-VMSF/ITO electrode, demonstrating high stability.

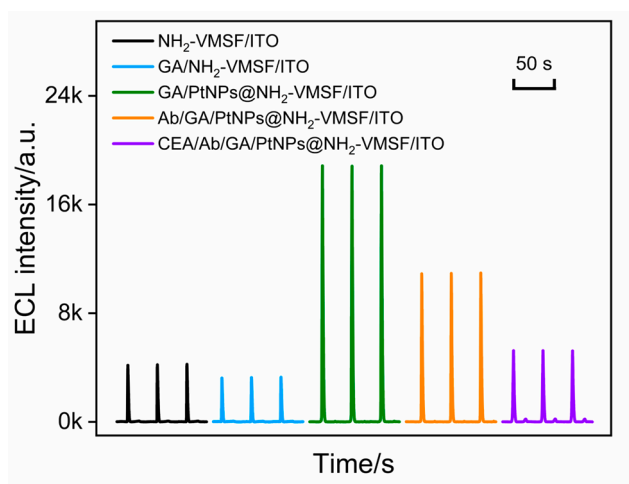
In order to verify the sensitization mechanism of PtNPs on the ECL of the luminol-H₂O₂ system, the possible reactive oxygen species (ROS) were investigated by adding various radical scavengers. As shown in Figure 4d, when the superoxide anion ($O_2^{\bullet-}$) scavenger benzoquinone (BQ) was added, the ECL signal significantly decreased. However, when the hydroxyl radical ($\cdot OH$) scavenger tert-butanol (TBA) was present, the ECL signal of the system remained relatively constant. This indicates that the ROS involved in this ECL process is $O_2^{\bullet-}$. A possible ECL mechanism during a CV scan in the presence of nanocatalysis is illustrated in the following equations. Briefly, luminol loses a proton to form the luminate anion (LH^-), which then loses an electron during the electrochemical oxidation process to generate the luminol radical ($L^{\bullet-}$). H₂O₂ is electrochemically catalyzed by PtNPs to produce a large amount of $O_2^{\bullet-}$, which reacts with $L^{\bullet-}$ to form the excited

state of 3-aminophthalate (AP^{2-*}). The emission of ECL occurs during the transition of the excited state back to the ground state (AP^{2-}).

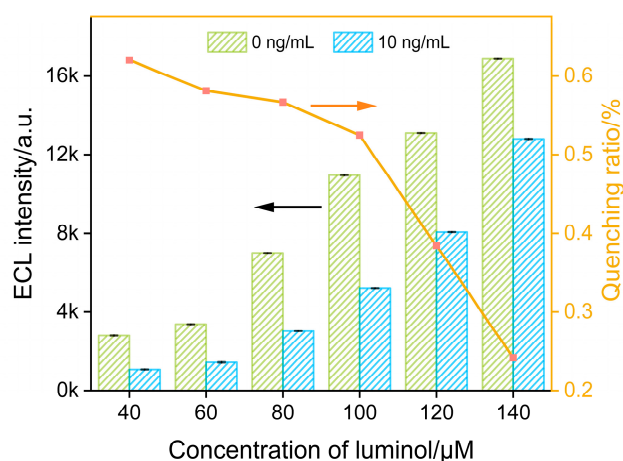


2.5. Feasibility of Immunosensor Fabrication and Optimization of CEA Detection Conditions

The feasibility of immunosensor fabrication was examined by investigating the ECL signals of the obtained electrodes during the construction process. As shown in Figure 5a, the ECL signal of the luminol- H_2O_2 system on the NH_2 -VMSF/ITO electrode is low. The modification of GA on the outer surface of SM@ NH_2 -VMSF and the following removal of SMs did not affect the ECL signal of the electrode. However, after the deposition of PtNPs inside the nanochannels, the ECL signal on the GA/PtNPs@ NH_2 -VMSF/ITO electrode was significantly enhanced. This enhancement is attributed to the electrocatalytic production of ROS by PtNPs towards H_2O_2 at negative potentials, thereby enhancing the ECL of the luminol. The covalent immobilization of Abs and the blocking of nonspecific sites by BSA resulted in a decrease in the ECL signal of the fabricated immunosensor (Ab/GA/PtNPs@ NH_2 -VMSF/ITO). Clearly, when Abs and the blocking BSA are immobilized on the outer surface of NH_2 -VMSF, they hinder the diffusion of luminol and H_2O_2 . In the presence of CEA in the system, the ECL signal of the electrode further decreases. This reduction is attributed to the specific recognition of CEA by the immunorecognition interface. As the immunocomplexes formed on the outer surface of NH_2 -VMSF, also on the exit of the nanochannels, they significantly hindered the diffusion of small molecules to the electrode surface, resulting in decreased ECL intensity.



(a)



(b)

Figure 5. Cont.

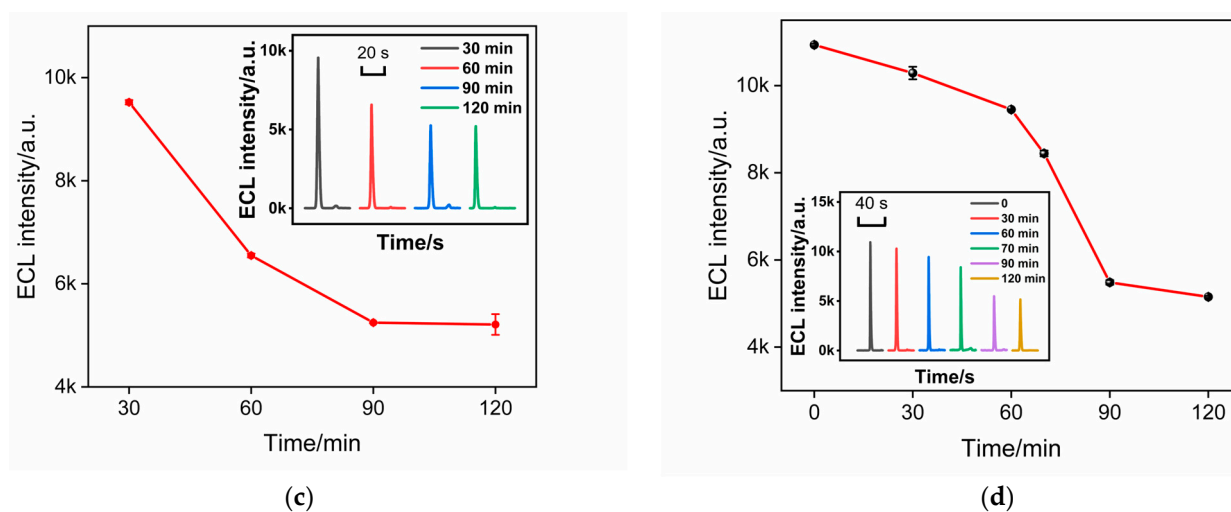


Figure 5. (a) ECL signal on different electrodes obtained in the fabrication of the immunosensor. (b) The ECL intensity and the proportion of ECL signal reduction caused by the gate effect in the luminol systems of different concentrations before and after adding CEA. (c) The ECL signal obtained after CEA binds with the immunosensor prepared using different incubation times for Ab immobilization. Inset is the corresponding ECL intensity. (d) The ECL intensity of the immunosensor obtained using different incubation times for CEA binding. Inset is the corresponding ECL intensity.

The concentration of ECL luminescent emitter is one of the factors influencing the gated signal. Thus, the effect of luminol concentration on CEA detection was investigated. Figure 5b shows the proportion of ECL signal reduction caused by the gate effect in the luminol systems of different concentrations before (I_0) and after (I) adding CEA. It can be observed that as the concentration of luminol increases, the absolute value of the ECL signal increases, but the quenching rate, calculated using $(I_0 - I)/I_0$, caused by the gate effect is low. The luminol concentration (100 μM) with the highest ECL quenching rate after CEA binding was selected for further investigation.

To achieve the highest sensitivity for the detection of CEA, the influence of antibody incubation time and CEA binding time on the performance of the immunosensor was also investigated. The ECL signal after the binding of CEA with immunosensors fabricated using different Ab immobilization times was investigated. As shown in Figure 6c, the ECL signal significantly decreased with the increase in the incubation time. After the antibody incubation time reached 90 min, the ECL signal reached a plateau. Thus, the antibody incubation time was chosen as 90 min in the subsequent experiments. In addition, when the CEA binding time with the immunorecognition interface reached 90 min, the ECL signal was the lowest. Thus, the binding time was set at 90 min.

2.6. ECL Determination of H_2O_2

Under optimal detection conditions, the performance of the constructed immune sensor for detecting CEA was investigated. Figure 6a shows the ECL–potential plots obtained on the Ab/GA/PtNPs@ NH_2 -VMSF/ITO electrodes in the presence of different concentrations of CEA. The ECL signal of the electrode after incubation with different concentrations of CEA is demonstrated in Figure 6b. As the CEA concentration increases, the number of immune complexes formed on the electrode surface increases. This leads to a stronger hindrance to the diffusion of the ECL emitters and co-reactants, resulting in a further decrease in the ECL signal of the electrode. Consequently, quantitative detection of CEA is achieved. Figure 6c shows the corresponding linear fitting curve. The results indicate a good linear relationship between the ECL signal (I_{ECL}) and the logarithm of CEA concentration ($\log C_{\text{CEA}}$) in the range of 0.1 pg mL^{-1} to 1000 ng mL^{-1} ($I_{\text{ECL}} = -1015 \log C_{\text{CEA}} + 6261$, $R^2 = 0.996$). The limit of detection (LOD), calculated based on a signal-to-noise ratio (S/N) of 3, was determined to be 0.3 pg mL^{-1} .

As a comparison, the performance of the immunosensor constructed using an NH_2 -VMSF/ITO electrode for detecting CEA was also investigated. As shown in Figure 6c, the linear range for CEA detection is from 1 pg mL^{-1} to 1 ng mL^{-1} ($I_{\text{ECL}} = -135 \log C_{\text{CEA}} + 595$, $R^2 = 0.999$). It is evident that the introduction of PtNPs as nanocatalysts enhances the ECL signal and significantly improves the detection linear range and sensitivity of the immunosensor.

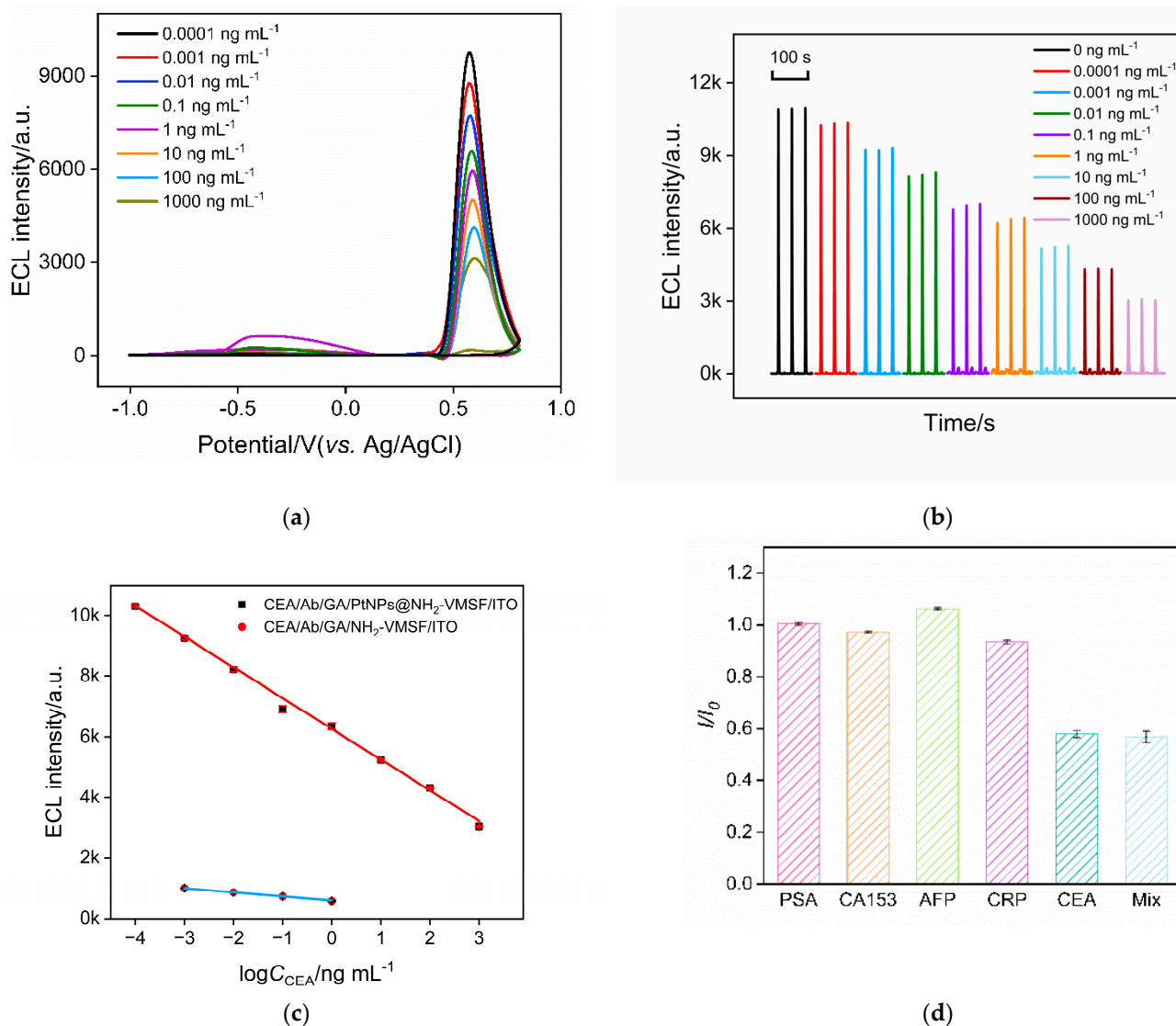


Figure 6. (a) ECL–potential plots obtained on Ab/GA/PtNPs@NH₂-VMSF/ITO electrode in presence of different concentrations of CEA. (b) ECL signal obtained on the fabricated immunosensor after incubation with different concentrations of CEA. (c) The linear fitting curve for the detection of CEA using Ab/GA/PtNPs@NH₂-VMSF/ITO (the line above) or Ab/GA/NH₂-VMSF/ITO electrode (the line below). (d) The change ratio of ECL signal in absence (I_0) or presence (I) of different species. The concentration of PSA, AFP, CRP, CEA is 1 ng mL^{-1} , and the concentration of CA15-3 is 1 mU mL^{-1} .

2.7. Selectivity and Real Sample Analysis

The common tumor biomarkers, including prostate specific antigen (PSA), carbohydrate antigen 15-3 (CA153), alpha-fetoprotein (AFP), and C-reactive protein (CRP), were selected as potential interferences to investigate the selectivity of the immunosensor. As shown in Figure 6d, these tumor biomarkers did not cause a significant change in the ECL signal of the immunosensor except when CEA was present. This indicates that the prepared immunosensor exhibits excellent selectivity.

The reliability of the fabricated immunosensor was assessed by detecting CEA in real serum samples. Five human serum samples (healthy, female) were detected. The concentrations of CEA detected by the constructed immunosensor were found to be $1.87 \pm 0.03 \text{ ng mL}^{-1}$, $0.69 \pm 0.02 \text{ ng mL}^{-1}$, $2.36 \pm 0.07 \text{ ng mL}^{-1}$, $1.10 \pm 0.03 \text{ ng mL}^{-1}$, $2.88 \pm 0.10 \text{ ng mL}^{-1}$ (mean \pm SD, $n = 3$), and they closely match the results ($1.95 \pm 0.04 \text{ ng mL}^{-1}$, $0.77 \pm 0.02 \text{ ng mL}^{-1}$, $2.28 \pm 0.06 \text{ ng mL}^{-1}$, $1.17 \pm 0.04 \text{ ng mL}^{-1}$, $2.83 \pm 0.09 \text{ ng mL}^{-1}$) obtained using the commercially used ECL analyzer (Cobas 6000, Roche, Basel, Switzerland). In addition, the accuracy of the detection was evaluated using a standard addition method. Commonly, the CEA concentration of a healthy person is less than 5 ng mL^{-1} . Different concentrations of CEA were added to the serum to simulate the blood samples of cancer patients ($> 5 \text{ ng mL}^{-1}$). As shown in Table 1, the recovery rate of the detection ranged from 98.7% to 107%, and the relative standard deviation (RSD) of the determination was no higher than 3.2%, demonstrating the accuracy of the determination.

Table 1. Detection of CEA in serum sample using standard addition method.

Sample	Spiked ^b (ng mL ⁻¹)	Found (ng mL ⁻¹)	RSD (%, $n = 3$)	Recovery (%)
Serum ^a	5.00	5.15	2.3	103
	10.0	9.92	0.8	99.2
	50.0	51.2	2.1	102.4
	100	98.7	1.4	98.7
	500	535	3.2	107

^a Samples with added CEA were diluted by a factor of 50 using the electrolyte. ^b The concentration of CEA was the added concentration before dilution.

3. Materials and Methods

3.1. Chemicals and Materials

Hexahydrate chloroplatinic acid ($\text{H}_2\text{PtCl}_6 \cdot 6\text{H}_2\text{O}$), luminol, sodium dihydrogen phosphate dihydrate ($\text{NaH}_2\text{PO}_4 \cdot 2\text{H}_2\text{O}$), disodium hydrogen phosphate dodecahydrate ($\text{Na}_2\text{HPO}_4 \cdot 12\text{H}_2\text{O}$), tetraethoxysilane (TEOS, 98%), cetyltrimethylammonium bromide (CTAB), 3-aminopropyltriethoxysilane (APTES), sodium hydroxide (NaOH), bovine serum albumin (BSA) were purchased from Shanghai Aladdin Biochemical Technology Co., Ltd. (Shanghai, China). Sulfuric acid, acetone, anhydrous ethanol (99.8%), and concentrated hydrochloric acid (HCl, 38%) were obtained from Hangzhou Shuanglin Reagent Co., Ltd. (Hangzhou, China). Carcinoembryonic antigen (CEA), anti-CEA antibody, alpha-fetoprotein (AFP), and cancer antigen 15-3 (CA 15-3) were purchased from Beijing Key Laboratory Biotechnologies Co., Ltd. (Beijing, China). C-reactive protein (CRP) was purchased from Nanjing OE Biotech Co., Ltd. (Nanjing, China). Prostate-specific antigen (PSA) was purchased from Beijing Boko Biotechnology Co., Ltd. (Beijing, China). Phosphate-buffered saline (PBS, 0.01 M, pH = 7.4) was prepared by mixing sodium dihydrogen phosphate and disodium hydrogen phosphate in certain proportions. All antigen samples were gradually diluted in PBS (0.01 M, pH = 7.4). All chemical reagents used were of analytical grade. Ultrapure water ($18.2 \text{ M}\Omega \cdot \text{cm}$) was used for the preparation of all solutions during the experiment. Indium tin oxide (ITO) conductive glass (square resistance $< 17 \Omega/\text{sq}$, ITO thickness: $100 \pm 20 \text{ nm}$) was purchased from Zhuhai Kaiwei Optoelectronics Technology Co., Ltd. (Zhuhai, China).

3.2. Characterizations and Instrumentations

Transmission electron microscopy (TEM, Hitachi HT7700) and scanning electron microscopy (SEM, Zeiss ULTRA 55) were used to characterize the morphology of VMSF and PtNPs. For TEM sample preparation, the VMSF layer was carefully scraped off the electrode using a knife and dispersed in anhydrous ethanol for ultrasonic dispersion. The resulting dispersion was drop-casted onto a copper grid. After being air dried, the sample was characterized at an accelerating voltage of 200 kV. For SEM sample preparation, NaOH

(2 M, 50 μ L) was drop-casted onto the surface of PtNPs@VMSF/ITO to etch the VMSF. After reaction for 5 min, NaOH on the surface was slowly rinsed off with ultrapure water, and the resulting material was left to air dry. Cyclic voltammetry (CV) testing was performed on an electrochemical workstation (CHI660D, Shanghai Chenhua, Shanghai, China). X-ray photoelectron spectroscopy (XPS) analysis was conducted using a PHI5300 electron spectrometer (PE Ltd., Cincinnati, OH, USA) with Mg K α radiation source (250 W, 14 kV). All experiments employed a traditional three-electrode system with Ag/AgCl serving as the reference electrode, platinum wire as the counter electrode, and the modified electrode as the working electrode.

3.3. Preparation of NH₂-VMSF/ITO and PtNPs@NH₂-VMSF/ITO Electrode

The electrochemical-assisted self-assembly (EASA) method reported in the literature was used to grow amino-functionalized vertically ordered mesoporous silica film (NH₂-VMSF) on the surface of indium tin oxide (ITO) electrode [52,53]. Briefly, ethanol (20 mL), sodium nitrate solution (0.1 M, pH = 2.36, 20 mL), CTAB (1.585 g), and APTES (318 μ L) were mixed. After uniform mixing, the pH of the solution was adjusted to 2.97 with HCl, and TEOS (2732 μ L) was then added to the solution. Under vigorous stirring, the obtained precursor solution was allowed to react for 2.5 h. After soaking ITO in a sodium hydroxide solution (1 M) for 60 min, it was sequentially washed with acetone, ethanol, and ultrapure water to give it a negatively charged surface. The ITO electrode was then cut, and an insulating adhesive was used to limit the electrode area to 0.5 cm \times 1 cm. Using ITO as the working electrode, a constant current (current density of -0.7 mA/cm²) was applied for 10 s to achieve rapid growth of NH₂-VMSF, followed by a quick rinse with a large amount of ultrapure water. The resulting electrode was dried with nitrogen gas and aged overnight at 120 $^{\circ}$ C to obtain an electrode with surfactant micelles (SMs) within the nanochannels, denoted as (SM@NH₂-VMSF/ITO). Finally, the SM@NH₂-VMSF/ITO electrode was immersed in a HCl-ethanol solution (0.1 M) and stirred for 5 min to remove the micelles, resulting in an electrode with open channels, abbreviated as NH₂-VMSF/ITO electrode.

The PtNPs@NH₂-VMSF/ITO electrode was prepared by electrodepositing H₂PtCl₆ in situ within the nanochannels of NH₂-VMSF. Briefly, an H₂PtCl₆ solution (3.86 mM in 0.1 M H₂SO₄) was used as the electrodepositing solution. The NH₂-VMSF/ITO electrode was subjected to a constant potential of -0.2 V for 2 s, resulting in the growth of PtNPs exclusively within the nanochannels. The electrode with PtNPs confined to the nanochannels was denoted as PtNPs@NH₂-VMSF/ITO.

3.4. Preparation of the Immunosensor

To prepare the immunosensor, PtNPs@NH₂-VMSF/ITO electrode was used as the substrate electrode. When constructing the immunosensing interface, glutaraldehyde (GA) was used as a cross-linking agent, and the CEA antibody (Ab) was immobilized through covalent cross-linking. To ensure that GA only modified the outer surface of NH₂-VMSF, the amino groups on the outer surface of NH₂-VMSF were treated with aldehyde derivatization before removing the SM. Firstly, GA solution (5%, 50 μ L) was drop-coated on the surface of SM@NH₂-VMSF/ITO electrode, followed by incubation at 37 $^{\circ}$ C in the dark for 30 min. Then, the electrode was thoroughly rinsed and then immersed in HCl-ethanol solution (0.1 M) for 5 min with stirring to remove micelles, resulting in an electrode with open channels, namely GA/NH₂-VMSF/ITO electrode. Next, PtNPs were electrodeposited inside the nanochannels following the above steps, resulting in GA/PtNPs@NH₂-VMSF/ITO electrode. Then, the electrode was immersed in Ab solution (100 μ g/mL) and incubated at 4 $^{\circ}$ C for 90 min. After the reaction, the electrode surface was washed with PBS solution (0.01 M, pH = 7.4) to remove unbound antibodies, and the electrode was then immersed in BSA solution (1%, *w/w*) at 4 $^{\circ}$ C for 90 min to block nonspecific binding sites. Finally, after thorough rinsing of the electrode, the immunosensor named BSA/Ab/GA/PtNPs@NH₂-VMSF/ITO was obtained.

3.5. ECL Detection of CEA

The detection performance of the immunosensor was evaluated by detecting different concentrations of CEA. The medium for the binding between the immuno-recognitive interface with CEA was PBS (0.01 M, pH = 7.4). Briefly, the electrode was incubated with different concentrations of CEA at 4 °C for 90 min. After thorough washing to remove unbound CEA, ECL testing was performed. Specifically, the electrolyte solution for detection was PBS (0.01 M, pH = 7.4) containing luminol (100 µM) and H₂O₂ (100 µM). Continuous scanning was conducted using the CV method on the working electrode within the potential ranged from −1 V to 0.8 V using a scan rate of 100 mV/s. CV curve and ECL response curve were simultaneously recorded.

4. Conclusions

In summary, an ECL immunosensing platform has been developed based on a 3D rigid nanochannel array film for the highly sensitive detection of the tumor marker CEA. The amino-modified VMSF was prepared in a one-step process on inexpensive and readily available ITO electrodes. The nanochannel array and outer surface were utilized as independent functional domains. The amino groups within the nanochannel array served as anchoring groups for the in situ growth of the platinum nanoparticles, which catalyzed hydrogen peroxide to produce ROS, significantly enhancing the ECL signal of the luminol with high stability. The amino groups on the outer surface were used as chemical reaction groups to covalently immobilize the antibodies after aldehyde derivatization, creating an immunorecognition interface. When CEA specifically bound to the immunorecognition interface, the resulting immunocomplexes reduced the diffusion of luminescent species and co-reactants towards the electrode, leading to a gating effect. By combining the specific recognition of antibodies and the enhanced ECL signal using the platinum nanoparticles, the constructed immunosensor achieved highly sensitive detection of CEA. The immunosensor offers advantages, such as inexpensive and readily available electrode substrates, a simple fabrication, an enhanced ECL signal, and selective recognition interfaces, making it highly promising for applications in tumor marker detection and other biological analyses.

Author Contributions: Investigation, H.Z. and C.Z.; data curation, H.Z., H.Q. and C.Z.; writing—original draft preparation, H.Z.; conceptualization and supervision, H.Z. and F.X.; writing—review and editing, C.Z., H.Q. and F.X. All authors have read and agreed to the published version of the manuscript.

Funding: This study was funded by the Zhejiang Provincial Natural Science Foundation of China (LY19B050008) and the Fundamental Research Funds of Zhejiang Sci-Tech University ZSTU (2020Q044).

Institutional Review Board Statement: Not applicable.

Informed Consent Statement: Not applicable.

Data Availability Statement: The data presented in this study are available on request from the corresponding author.

Conflicts of Interest: The authors declare no conflict of interest.

Sample Availability: Not applicable.

References

1. Cristaudo, A.T.; Jennings, S.B.; Morris, D.L. Comparison of proportion of elevated carcinoembryonic antigen levels in patients with appendiceal and colorectal adenocarcinoma: A systematic review and meta-analysis. *Anticancer Res.* **2022**, *42*, 4217–4235. [[CrossRef](#)] [[PubMed](#)]
2. Ng, S.S.; Lee, H.L.; Raja, P.B.; Doong, R.A. Recent advances in nanomaterial-based optical biosensors as potential point-of-care testing (PoCT) probes in carcinoembryonic antigen detection. *Chem. Asian J.* **2022**, *17*, e202200287.
3. Mao, C.; Wu, L.; Wen, Y.; Tang, X.; Huang, Z.; Zhao, L. Photoelectrochemical immunosensor for carcinoembryonic antigen detection—an attempt for early cancer screening. *Biosens. Bioelectron.* **2023**, *220*, 114918. [[CrossRef](#)] [[PubMed](#)]

4. Shi, B.J.; Shang, L.; Zhang, W.; Jia, L.P.; Ma, R.N.; Xue, Q.W.; Wang, H.S. Electrochemical stripping chemiluminescent sensor based on copper nanoclusters for detection of carcinoembryonic antigen. *Sens. Actuators B Chem.* **2021**, *344*, 130291. [[CrossRef](#)]
5. Zhou, X.; Han, Q.; Zhou, J.; Liu, C.; Liu, J. Reagentless electrochemical detection of tumor biomarker based on stable confinement of electrochemical probe in bipolar silica nanochannel film. *Nanomaterials* **2023**, *13*, 1645. [[CrossRef](#)]
6. Wu, Z.; Lu, J.; Fu, Q.; Sheng, L.; Liu, B.; Wang, C.; Li, C.; Li, T. A smartphone-based enzyme-linked immunochromatographic sensor for rapid quantitative detection of carcinoembryonic antigen. *Sens. Actuators B Chem.* **2021**, *329*, 129163. [[CrossRef](#)]
7. Han, R.; Sun, Y.; Dai, Y.; Gao, D.; Wang, X.; Luo, C. A chemiluminescence aptasensor for sensitive detection of carcinoembryonic antigen based on dual aptamer-conjugates biorecognition. *Sens. Actuators B Chem.* **2021**, *326*, 128833. [[CrossRef](#)]
8. Liao, X.; Wang, X.; Sun, C.; Chen, S.; Zhang, M.; Mei, L.; Qi, Y.; Hong, C. Ratiometric electrochemical immunosensor triggered by an advanced oxidation process for the ultrasensitive detection of carcinoembryonic antigen. *Sens. Actuators B Chem.* **2022**, *362*, 131804. [[CrossRef](#)]
9. Li, J.; Zhao, L.; Wang, W.; Liu, Y.; Yang, H.; Kong, J.; Si, F. Polymer-functionalized carbon nanotubes prepared via ring-opening polymerization for electrochemical detection of carcinoembryonic antigen. *Sens. Actuators B Chem.* **2021**, *328*, 129031. [[CrossRef](#)]
10. Yan, Z.; Zhang, S.; Liu, J.; Xing, J. Homogeneous electrochemical aptamer sensor based on two-dimensional nanocomposite probe and nanochannel modified electrode for sensitive detection of carcinoembryonic antigen. *Molecules* **2023**, *28*, 5186. [[CrossRef](#)] [[PubMed](#)]
11. Lin, J.; Li, K.; Wang, M.; Chen, X.; Liu, J.; Tang, H. Reagentless and sensitive determination of carcinoembryonic antigen based on a stable Prussian blue modified electrode. *RSC Adv.* **2020**, *10*, 38316–38322. [[CrossRef](#)] [[PubMed](#)]
12. Liu, G.; Gao, H.; Chen, J.; Shao, C.; Chen, F. An ultra-sensitive electrochemiluminescent detection of carcinoembryonic antigen using a hollowed-out electrode. *Electroanalysis* **2021**, *33*, 1444–1450. [[CrossRef](#)]
13. Gong, J.; Zhang, T.; Chen, P.; Yan, F.; Liu, J. Bipolar silica nanochannel array for dual-mode electrochemiluminescence and electrochemical immunosensing platform. *Sens. Actuators B Chem.* **2022**, *368*, 132086. [[CrossRef](#)]
14. Dong, J.; Feng, J. Electrochemiluminescence from single molecule to imaging. *Anal. Chem.* **2023**, *95*, 374–387. [[CrossRef](#)] [[PubMed](#)]
15. Huang, J.; Zhang, T.; Zheng, Y.; Liu, J. Dual-mode sensing platform for cancer antigen 15-3 determination based on a silica nanochannel array using electrochemiluminescence and electrochemistry. *Biosensors* **2023**, *13*, 317. [[CrossRef](#)] [[PubMed](#)]
16. Chen, H.; Huang, J.; Zhang, R.; Yan, F. Dual-mode electrochemiluminescence and electrochemical sensor for alpha-fetoprotein detection in human serum based on vertically ordered mesoporous silica films. *Front. Chem.* **2022**, *10*, 1023998. [[CrossRef](#)] [[PubMed](#)]
17. Luo, X.; Zhang, T.; Tang, H.; Liu, J. Novel electrochemical and electrochemiluminescence dual-modality sensing platform for sensitive determination of antimicrobial peptides based on probe encapsulated liposome and nanochannel array electrode. *Front. Nutr.* **2022**, *9*, 962736. [[CrossRef](#)] [[PubMed](#)]
18. Liang, R.; Jiang, J.; Zheng, Y.; Sailjoi, A.; Chen, J.; Liu, J.; Li, H. Vertically oriented mesoporous silica film modified fluorine-doped tin oxide electrode for enhanced electrochemiluminescence detection of lidocaine in serum. *RSC Adv.* **2021**, *11*, 34669–34675. [[CrossRef](#)]
19. Liu, Z.; Qi, W.; Xu, G. Recent advances in electrochemiluminescence. *Chem. Soc. Rev.* **2015**, *44*, 3117–3142. [[CrossRef](#)]
20. Niu, Q.; Fu, L.; Zhong, Y.; Cui, B.; Zhang, G.; Yang, Y. Sensitive and specific detection of carcinoembryonic antigens using toroidal metamaterial biosensors integrated with functionalized gold nanoparticles. *Anal. Chem.* **2022**, *95*, 1123–1131. [[CrossRef](#)] [[PubMed](#)]
21. Sun, J.; Sun, H.; Liang, Z. Nanomaterials in electrochemiluminescence sensors. *ChemElectroChem* **2017**, *4*, 1651–1662. [[CrossRef](#)]
22. Chen, Y.; Zhou, S.; Li, L.; Zhu, J.J. Nanomaterials-based sensitive electrochemiluminescence biosensing. *Nano Today* **2017**, *12*, 98–115. [[CrossRef](#)]
23. Gong, J.; Tang, H.; Wang, M.; Lin, X.; Wang, K.; Liu, J. Novel three-dimensional graphene nanomesh prepared by facile electro-etching for improved electroanalytical performance for small biomolecules. *Mater. Design* **2022**, *215*, 110506. [[CrossRef](#)]
24. Xu, S.; Zhang, S.; Li, Y.; Liu, J. Facile synthesis of iron and nitrogen co-doped carbon dot nanozyme as highly efficient peroxidase mimics for visualized detection of metabolites. *Molecules* **2023**, *28*, 6064. [[CrossRef](#)] [[PubMed](#)]
25. Shang, L.; Shi, B.J.; Zhang, W.; Jia, L.P.; Ma, R.N.; Xue, Q.W.; Wang, H.S.; Yan, W. Electrochemical stripping chemiluminescence coupled with recycling amplification strategy for sensitive detection of carcinoembryonic antigen. *Sens. Actuators B Chem.* **2022**, *368*, 132191. [[CrossRef](#)]
26. Li, X.; Zhou, L.; Ding, J.; Sun, L.; Su, B. Platinized silica nanoporous membrane electrodes for low-fouling hydrogen peroxide detection. *ChemElectroChem* **2020**, *7*, 2081–2086. [[CrossRef](#)]
27. Chu, X.; Duan, D.; Shen, G.; Yu, R. Amperometric glucose biosensor based on electrodeposition of platinum nanoparticles onto covalently immobilized carbon nanotube electrode. *Talanta* **2007**, *71*, 2040–2047. [[CrossRef](#)] [[PubMed](#)]
28. Dong, X.Y.; Mi, X.N.; Zhang, L.; Liang, T.M.; Xu, J.J.; Chen, H.Y. DNAzyme-functionalized Pt nanoparticles/carbon nanotubes for amplified sandwich electrochemical DNA analysis. *Biosens. Bioelectron.* **2012**, *38*, 337–341. [[CrossRef](#)]
29. Zhang, H.; Li, B.; Sun, Z.; Zhou, H.; Zhang, S. Integration of intracellular telomerase monitoring by electrochemiluminescence technology and targeted cancer therapy by reactive oxygen species. *Chem. Sci.* **2017**, *8*, 8025–8029. [[CrossRef](#)]
30. Zhang, C.; Jiang, H.; Ma, R.; Zhang, Y.; Chen, Q. Simple non-enzymatic electrochemical sensor for hydrogen peroxide based on nafion/platinum nanoparticles/reduced graphene oxide nanocomposite modified glassy carbon electrode. *Ionics* **2017**, *23*, 1309–1317. [[CrossRef](#)]

31. Chen, M.; Xie, X.; Wang, Y.; Pang, X.; Jia, Z. Hollow silica nanotubes for space-confined synthesis of noble metal nanorods and nanopeapods. *ACS Appl. Nano Mater.* **2021**, *4*, 6075–6082. [[CrossRef](#)]
32. Zhang, C.; Shi, X.K.; Wu, C.D. Stabilization of NiO/NiII heterojunctions inside robust porous metal silicate materials for high-performance catalysis. *Inorg. Chem.* **2022**, *61*, 16786–16793. [[CrossRef](#)]
33. Zhou, P.; Yao, L.; Su, B. Fabrication, characterization, and analytical application of silica nanopore array-modified platinum electrode. *ACS Appl. Mater. Interfaces* **2019**, *12*, 4143–4149. [[CrossRef](#)]
34. Amouzadeh Tabrizi, M.; Acedo, P. Highly sensitive aptasensor for the detection of SARS-CoV-2-RBD using aptamer-gated methylene blue@mesoporous silica film/laser engraved graphene electrode. *Biosens. Bioelectron.* **2022**, *215*, 114556. [[CrossRef](#)]
35. Yan, F.; Chen, J.; Jin, Q.; Zhou, H.; Sailjoi, A.; Liu, J.; Tang, W. Fast one-step fabrication of a vertically-ordered mesoporous silica-nanochannel film on graphene for direct and sensitive detection of doxorubicin in human whole blood. *J. Mater. Chem. C* **2020**, *8*, 7113–7119. [[CrossRef](#)]
36. Zheng, W.; Su, R.; Lin, X.; Liu, J. Nanochannel array modified three-dimensional graphene electrode for sensitive electrochemical detection of 2,4,6-trichlorophenol and prochloraz. *Front. Chem.* **2022**, *10*, 954802. [[CrossRef](#)] [[PubMed](#)]
37. Teng, Z.; Zheng, G.; Dou, Y.; Li, W.; Mou, C.Y.; Zhang, X.; Asiri, A.M.; Zhao, D. Highly ordered mesoporous silica films with perpendicular mesochannels by a simple stöber-solution growth approach. *Angew. Chem. Int. Ed.* **2012**, *51*, 2173–2177. [[CrossRef](#)]
38. Zhang, T.; Yang, L.; Yan, F.; Wang, K. Vertically-ordered mesoporous silica film based electrochemical aptasensor for highly sensitive detection of alpha-fetoprotein in human serum. *Biosensors* **2023**, *13*, 628. [[CrossRef](#)]
39. Zhang, M.; Zou, Y.; Zhou, X.; Yan, F.; Ding, Z. Vertically-ordered mesoporous silica films for electrochemical detection of Hg(II) ion in pharmaceuticals and soil samples. *Front. Chem.* **2022**, *10*, 952936. [[CrossRef](#)]
40. Zhang, T.; Xu, S.; Lin, X.; Liu, J.; Wang, K. Label-free electrochemical aptasensor based on the vertically-aligned mesoporous silica films for determination of aflatoxin B1. *Biosensors* **2023**, *13*, 661. [[CrossRef](#)]
41. Liu, X.; Li, H.; Zhou, H.; Liu, J.; Li, L.; Liu, J.; Yan, F.; Luo, T. Direct electrochemical detection of 4-aminophenol in pharmaceuticals using ITO electrodes modified with vertically-ordered mesoporous silica-nanochannel films. *J. Electroanal. Chem.* **2020**, *878*, 114568. [[CrossRef](#)]
42. Walcarius, A.; Sibottier, E.; Etienne, M.; Ghanbaja, J. Electrochemically assisted self-assembly of mesoporous silica thin films. *Nat. Mater.* **2007**, *6*, 602–608. [[CrossRef](#)] [[PubMed](#)]
43. Deng, X.; Lin, X.; Zhou, H.; Liu, J.; Tang, H. Equipment of vertically-ordered mesoporous silica film on electrochemically pretreated three-dimensional graphene electrodes for sensitive detection of methidazine in urine. *Nanomaterials* **2023**, *13*, 239. [[CrossRef](#)] [[PubMed](#)]
44. Zou, Y.; Zhou, X.; Xie, L.; Tang, H.; Yan, F. Vertically-ordered mesoporous silica films grown on boron nitride-graphene composite modified electrodes for rapid and sensitive detection of carbendazim in real samples. *Front. Chem.* **2022**, *10*, 939510. [[CrossRef](#)] [[PubMed](#)]
45. Zheng, W.; Su, R.; Yu, G.; Liu, L.; Yan, F. Highly sensitive electrochemical detection of paraquat in environmental water samples using a vertically ordered mesoporous silica film and a nanocarbon composite. *Nanomaterials* **2022**, *12*, 3632. [[CrossRef](#)]
46. Yang, L.; Zhang, T.; Zhou, H.; Yan, F.; Liu, Y. Silica nanochannels boosting Ru(bpy)₃²⁺-mediated electrochemical sensor for the detection of guanine in beer and pharmaceutical samples. *Front. Nutr.* **2022**, *9*, 987442. [[CrossRef](#)] [[PubMed](#)]
47. Asadpour, F.; Mazloum-Ardakani, M.; Hoseynidokht, F.; Moshtaghoun, S.M. In situ monitoring of gating approach on mesoporous silica nanoparticles thin-film generated by the EASA method for electrochemical detection of insulin. *Biosens. Bioelectron.* **2021**, *180*, 113124. [[CrossRef](#)] [[PubMed](#)]
48. Vanheusden, G.; Philipsen, H.; Herregods, S.J.F.; Vereecken, P.M. Aggregate-free micrometer-thick mesoporous silica thin films on planar and three-dimensional structured electrodes by hydrodynamic diffusion layer control during electrochemically assisted self-assembly. *Chem. Mater.* **2021**, *33*, 7075–7088. [[CrossRef](#)]
49. Zhou, H.; Ma, X.; Sailjoi, A.; Zou, Y.; Lin, X.; Yan, F.; Su, B.; Liu, J. Vertical silica nanochannels supported by nanocarbon composite for simultaneous detection of serotonin and melatonin in biological fluids. *Sens. Actuators B Chem.* **2022**, *353*, 131101. [[CrossRef](#)]
50. Wang, K.; Yang, L.; Huang, H.; Lv, N.; Liu, J.; Liu, Y. Nanochannel array on electrochemically polarized screen printed carbon electrode for rapid and sensitive electrochemical determination of clozapine in human whole blood. *Molecules* **2022**, *27*, 2739. [[CrossRef](#)] [[PubMed](#)]
51. Han, Q.; Zhang, T.; Wang, M.; Yan, F.; Liu, J. Disposable Electrochemical Sensors for Highly Sensitive Detection of Chlorpromazine in Human Whole Blood Based on the Silica Nanochannel Array Modified Screen-Printed Carbon Electrode. *Molecules* **2022**, *27*, 8200. [[CrossRef](#)] [[PubMed](#)]
52. Cui, Y.; Zhang, S.; Zhou, X.; Yan, F.; Hu, W. Silica nanochannel array on co-electrodeposited graphene-carbon nanotubes 3D composite film for antifouling detection of uric acid in human serum and urine samples. *Microchem. J.* **2023**, *190*, 108632. [[CrossRef](#)]
53. Gong, J.; Zhang, T.; Luo, T.; Luo, X.; Yan, F.; Tang, W.; Liu, J. Bipolar silica nanochannel array confined electrochemiluminescence for ultrasensitive detection of SARS-CoV-2 antibody. *Biosens. Bioelectron.* **2022**, *215*, 114563. [[CrossRef](#)] [[PubMed](#)]

Disclaimer/Publisher's Note: The statements, opinions and data contained in all publications are solely those of the individual author(s) and contributor(s) and not of MDPI and/or the editor(s). MDPI and/or the editor(s) disclaim responsibility for any injury to people or property resulting from any ideas, methods, instructions or products referred to in the content.